

Cite this: *Energy Environ. Sci.*,
2026, **19**, 605

Metalloccenium salts as tunable dopants for enhanced efficiency of perovskite solar cells

Thomas Webb,^{†ab} Francesco Vanin,^{id†ac} Danpeng Gao,^{idc} Lei Zhu,^{idd} William D. J. Tremlett,^{ida} Amanz Azaden,^{ab} Alice Rodgers,^{ab} Polina Jacoutot,^{ab} Andrew J. P. White,^{ida} M. Saiful Islam,^{idd} Nicholas J. Long,^{ida} Zonglong Zhu,^{id*c} and Saif A. Haque^{id*ab}

The generation of free carriers through extrinsic doping is essential for transforming the electronic properties of organic semiconductors (OSCs). Doped OSCs play a crucial role in the successful operation of a wide range of electrical and optoelectronic devices, but challenges remain associated with dopant design, such as processability, stability and efficacy. Herein, we introduce a class of versatile p-type dopants based on metalloccenium salts with the general formula $([M(C_{10}H_{10-n})(X)_n]^+[Y]^-)$ that meet these requirements. Critical to this approach is the ability to independently tune the cation *via* the redox-active metal cation (M) and the functionality (X) on the cyclopentadiene ring, allowing control over the oxidation strength. Simultaneously, the ability to tune the counter-anion (Y) allows control over the doping efficacy and stability of the resultant doped OSC⁺ salt. In this study, we systematically investigate the effect of cation and anion structures on the doping of OSCs and elucidate structure–property relationships for dopant design. We unravel the doping mechanism and demonstrate that such dopants can be used to enhance the hole extraction yield by 45% at perovskite/OSC heterojunctions. Perovskite/OSC photoactive layers using metalloccenium dopants show significantly increased tolerance to moisture induced degradation as compared to films using conventional LiTFSI based dopants. Finally, we showcase the use of our optimised ferrocenium dopant in n–i–p configuration perovskite solar cells, demonstrating LiTFSI-free and additive-free devices with impressive solar-light to electrical power conversion efficiencies reaching 25.30%.

Received 16th September 2025,
Accepted 2nd December 2025

DOI: 10.1039/d5ee05482f

rsc.li/ees

Broader context

Organic semiconductors (OSCs) are critical components of next-generation electronics, enabling the development of low-cost, lightweight devices that surpass current technologies in fields spanning light-emitting diodes, field-effect transistors, thermoelectrics, and photovoltaics. The key to realising the beneficial electronic properties of OSCs is the use of chemical dopants, making the doping method critical for device performance and commercialisation. However, issues with dopant design remain, including poor processability, limited tunability, and chemical instability, restricting performance and stability. Herein, we introduce a design strategy for molecular dopants based on metalloccenium salts, elucidating structure–property relationships to guide independent tuning of redox potential and counter-anion interactions. This approach provides precise control over doping strength and stability, establishing design rules for doping OSCs. As a case study, we apply these air-stable dopants to perovskite solar cells (PSCs), replacing the hygroscopic and volatile lithium-based dopants typically used in the organic hole transport layer (HTL). Perovskite/HTL films containing our metalloccenium dopants show enhanced resistance to environmental degradation and improved interfacial charge separation. We report lithium-free and additive-free devices with efficiencies exceeding 25%, demonstrated using an archetypal HTL, namely spiro-OMeTAD. This work addresses the universal challenge of controlled and stable doping, providing a platform for durable, high-performance OSC devices across next-generation optoelectronics.

^a Department of Chemistry, Molecular Sciences Research Hub, Imperial College London, London, W12 0BZ, UK. E-mail: s.a.haque@imperial.ac.uk^b Centre for Processable Electronics, Molecular Sciences Research Hub, Imperial College London, London, W12 0BZ, UK^c Department of Chemistry, City University of Hong Kong, Kowloon, 999077, Hong Kong. E-mail: zongluzhu@cityu.edu.hk^d Department of Materials, University of Oxford, Oxford, OX1 3PH, UK

† These authors contributed equally.

Introduction

Chemical doping plays a critical role in tuning the intrinsic carrier conduction properties of organic semiconductors (OSCs).^{1–3} The increased carrier density in doped OSCs results in improved charge carrier mobility and enhanced conductivity. The use of doping as a means to improve the electronic



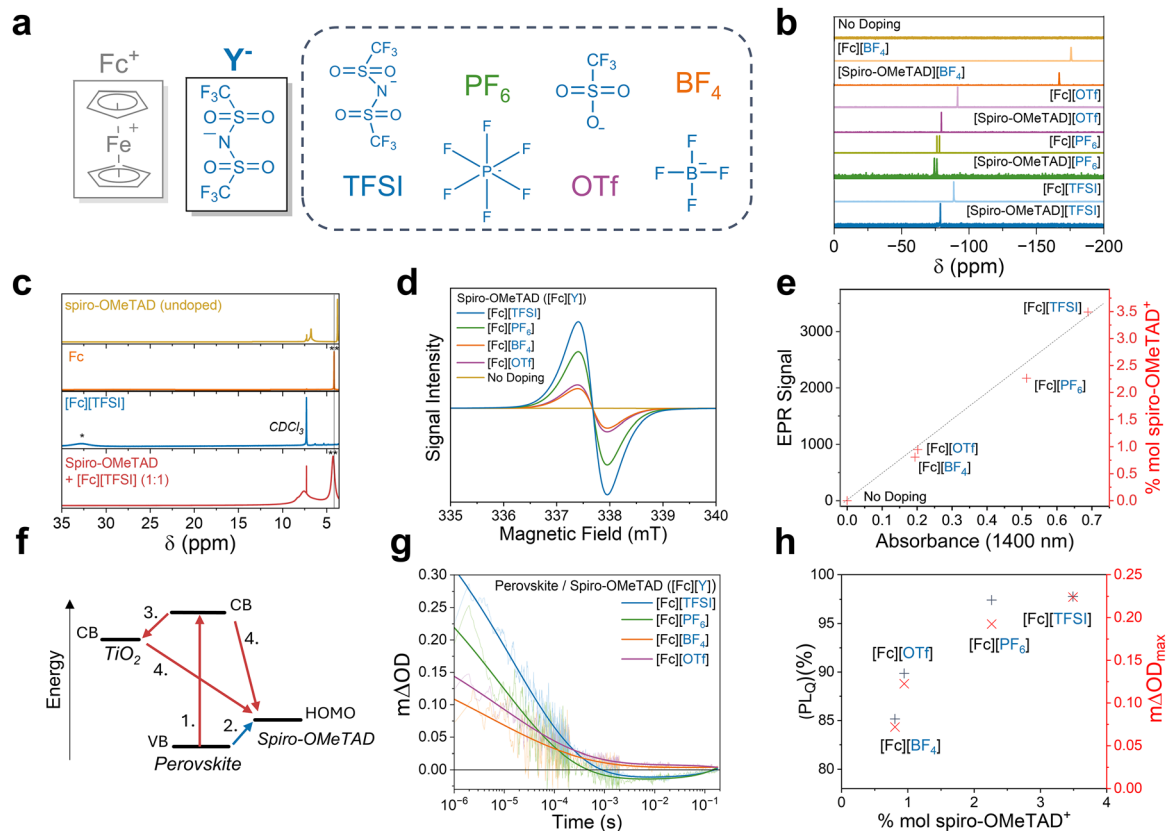


Fig. 2 Optimisation of the anion (Y^-) of $[M(C_{10}H_{10-n})(X)_n]^+[Y]^-$ dopants. (a) Chemical structures of anions from left to right: bis(trifluoromethylsulfoniomide) $[TFSI]^-$, hexafluorophosphate $[PF_6]^-$, trifluoromethylsulfimide $[OTf]^-$, and tetrafluoroborate $[BF_4]^-$. (b) ^{19}F NMR showing shifts in the anion chemical environment before and after addition to spiro-OMeTAD. (c) 1H NMR of pre-doped spiro-OMeTAD (yellow) with the reformation of the ferrocene (orange) Cp singlet upon addition of $[Fc][TFSI]$ (blue) to spiro-OMeTAD, forming $[spiro-OMeTAD]^+[TFSI]^-$ (red). (d) EPR data of spiro-OMeTAD doped with different ferrocenium salts and (e) correlation between EPR oxidation yield and absorbance of spiro-OMeTAD $^{+•}$ polarons at 1400 nm. (f) Key photoinduced charge transfer reactions at the TiO_2 /perovskite/spiro-OMeTAD heterojunction. Schematic of electron (red) and hole (blue) processes in a typical transient absorbance spectroscopy (TAS) experiment, (1) excitation of the perovskite sample to form electrons and holes. (2) Hole injection into spiro-OMeTAD, where the yield is directly proportional to ΔOD_{max} . (3) Electron injection into an electron transport layer (TiO_2). (4) Interfacial recombination between electrons in the conduction bands of perovskite and TiO_2 and holes injected into spiro-OMeTAD. (g) TAS of TiO_2 /MAPbI $_3$ /doped spiro-OMeTAD films. The yield of hole transfer at the MAPbI $_3$ /doped spiro-OMeTAD is proportional to the change in optical density ΔOD ($m\Delta OD = \Delta OD \times 10^{-3}$). In this study, the spiro-OMeTAD was doped with ferroceniums with different anions. (h) Comparison between the choice of ferrocenium anion species and the performance of a spiro-OMeTAD OSC.

resonance (EPR) enables the determination of the concentration of unpaired electrons through the magnitude of perturbation caused by an applied magnetic field.⁴⁴ EPR signals of ferrocenium compounds are not observed at the experimental temperature of 298 K owing to fast spin–lattice relaxations (SI, Fig. S10).⁴⁵ This simplification allows for correlation of the EPR double integral intensity as an estimate of the molar percentage of spiro-OMeTAD oxidation reported in Fig. 2d and e. From these data, we observe oxidation efficacies ranging from 0.77% in the BF_4 salt to 3.50% with the TFSI anion. These findings are in agreement with the UV-vis absorbance intensity of the spiro-OMeTAD $^{+•}$ polaron ($\lambda = 1400$ nm) (SI, Fig. S11). From the EPR and UV-vis studies, we establish a trend in anion doping efficacy following the order $BF_4 < OTf < PF_6 < TFSI$, shown in Fig. 2e.

Transient absorption spectroscopy (TAS) was used to probe the photoinduced hole transfer reaction at the MAPbI $_3$ perovskite/doped spiro-OMeTAD heterojunction.^{29,46–48} We determined

the kinetics of charge recombination between the photoexcited electrons in the perovskite and holes in the spiro-OMeTAD by monitoring the decay of the spiro-OMeTAD $^{+•}$ polarons at 1600 nm following pulsed laser excitation at 532 nm (Fig. 2f). Fig. 2g shows typical decay traces of hole polarons within spiro-OMeTAD as a function of dopant anion. We note that the TAS decays for the PF_6 and TFSI anions exhibit negative change in optical density (ΔOD) signals on millisecond time-scales; the origin and optimisation of these kinetics are discussed in greater detail below (*vide infra*). The ΔOD is directly related to the concentration of photogenerated spiro-OMeTAD $^{+•}$ and is therefore a measure of the yield of hole transfer. SI, Fig. S12 presents the relative hole transfer yield ΔOD_{max} (defined as ΔOD at 1 μs) for the different dopant anions. Photoluminescence (PL) quenching measurements (SI, Fig. S13) agree with the transient absorption data; samples with greater yield of PL quenching exhibit larger ΔOD_{max} values.⁴⁹ In summary, Fig. 2h presents a direct correlation



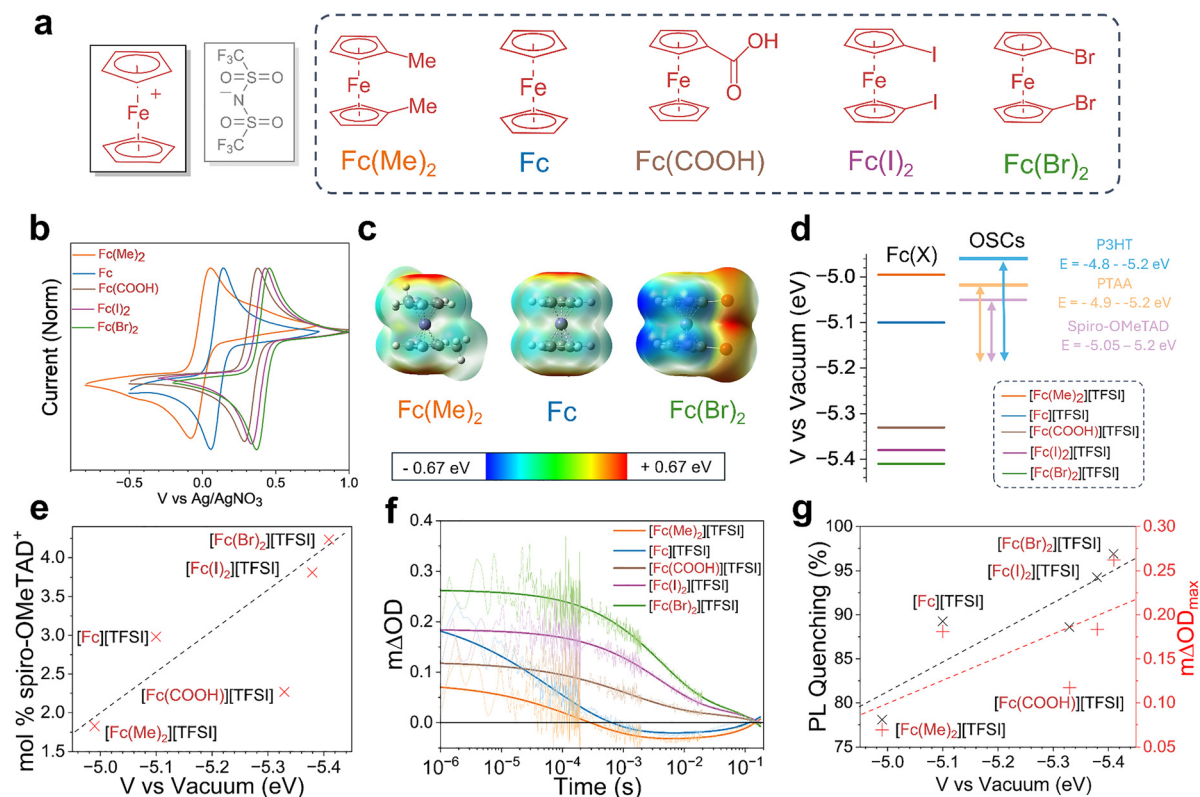


Fig. 3 Optimisation of the cation functionality (X) of $[(M)(C_5H_{5-n})_2(X)]^+[Y]^-$ dopants. (a) Chemical structures of ferrocene derivatives used to produce ferrocenium dopants. (b) Cyclic voltammetry (CV) measurements of ferrocene derivatives at 2 mM in 0.1 M $[nBu_4PF_6]$ ACN electrolyte against an $Ag/AgNO_3$ reference electrode. (c) DFT electronic surface potential (EPS) of the most electron-donating functionalised derivative $[Fc(Me)_2]$, ferrocene, and the most electron-withdrawing functionalised derivative $[Fc(Br)_2]$, red areas indicate areas of electronegativity. (d) Comparison of oxidation potential between ferrocene-derivatives and common OSC materials. (e) Comparison between the molar oxidation percentage of spiro-OMeTAD calculated from EPR spectroscopy against the vacuum potential of ferrocene-derivatives. (f) Transient absorption spectroscopy (TAS) studies of $TiO_2/MAPbI_3$ /doped spiro-OMeTAD films. TAS data showing changes in the hole extraction efficiency in spiro-OMeTAD doped with different ferrocenium cations. The change in optical density ΔOD is proportional to the yield of hole transfer (note that $m\Delta OD = \Delta OD \times 10^{-3}$). (g) Correlation between the performance of spiro-OMeTAD as an HTL and the oxidation potential of the ferrocenium cation used to dope.

solubility in chlorobenzene, which may rationalise the lower mol% oxidation observed.

We next investigate the influence of the cation functional groups on the performance of the doped OSC when used as an HTL. First, TAS was used to compare the yield of hole extraction from a perovskite active layer, providing a comparison between the performances of the different cations when used to dope spiro-OMeTAD. From the decays presented in Fig. 3f, the yield of hole transfer ($m\Delta OD_{max}$) was found to follow the same trend as observed in the EPR measurements, where the inclusion of electron-withdrawing substituents improved the hole extraction yield. Using $[Fc(Br)_2]^+$, we observe that the yield of hole transfer can be enhanced by 45%. In contrast, replacing the $[Fc]^+$ cation with the less oxidising $[Fc(Me)_2]^+$ cation decreased the hole transfer yield by 62%. These findings were further supported using PL spectroscopy (Fig. 3g and SI, Fig. S25), whereby greater quenching of the perovskite active layer was achieved using dopants with more electron-withdrawing ring substituents. As such, the design of the functionality on the Cp ring is critical in determining the performance of the doped OSC when used as a hole extraction layer (Fig. 3g).

We note the presence of a negative transient feature on the order of 10^{-2} s in spiro-OMeTAD in samples prepared with $[Fc(Me)_2]$ and $[Fc]$ cations. We further note that this feature was also observed in $[Fc][PF_6]$ doped samples (Fig. 2f). We attribute this feature to a temporary de-doping effect induced by the close energetic proximity between the Fc/Fc^+ redox potential and the first oxidation of spiro-OMeTAD combined with the reversible nature of the Fc/Fc^+ (<0.1 eV) (SI, Note S1). This transient effect is not observed using cations with a larger offset compared to the OSC, owing to the formation of a large energetic barrier to de-doping. Notably, while $[Fc(COOH)][TFSI]$ doped spiro-OMeTAD exhibits lower yields of hole transfer owing to poor solubility in chlorobenzene, the effect is still present, confirming that the process is driven by energetics.

Finally, we consider the influence of the neutral ferrocene that forms as a by-product of eqn (1). Formation of neutral ferrocene within the HTL can (i) improve the performance of the HTL and (ii) provide a hydrophobic alternative to hygroscopic metal cations, such as Li^+ .^{29,53} In synergy with the experimental work, we used DFT and *ab initio* molecular dynamics methods to gain insights into ferrocene-perovskite



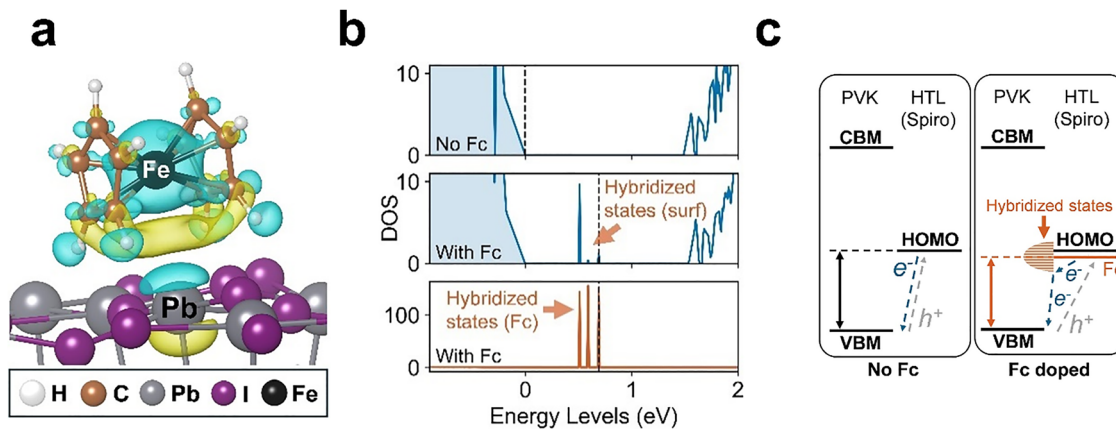


Fig. 4 DFT modelling of the impact of residual ferrocene, the by-product of ferrocenium doping. (a) Side view of the simulated lowest-energy configuration of ferrocene on the (001) PbI_2 -terminated MAPbI_3 surface and charge density profile (with charge density gain and loss coloured in yellow and blue, respectively). (b) Calculated electronic density of states (DOS) for the MAPbI_3 surface with and without Fc doping. DOS are projected onto atoms in the top three layers of the surface slab (blue) and onto ferrocene atoms (orange). Top panel: surface without ferrocene; middle and bottom panels: surfaces with the ferrocene molecule relaxed near the surface, showing additional hybridized states not found in the undoped system. All DOS plots are aligned to the surface VBM, set to zero on the energy axis. The black dashed line indicates the position of the highest occupied level at the surface. (c) Schematic energy level diagram illustrating the proposed mechanism of hole transport at the interface between the perovskite (PVK) layer and the HTL without (left) and with (right) Fc doping.

surface interactions, which are not fully understood on the atomic scale. For such a detailed modelling analysis, ferrocene provides a simple representative system, allowing us to consider the behaviour of the dopant by-product at the perovskite interface. The simulations examined the atomistic effects at the (001) PbI_2 -terminated surfaces of MAPbI_3 , as it is one of the most stable perovskite facets (computational details are provided in the Methods section).

Four important results emerged. First, the ferrocene molecule adsorbs favourably on the MAPbI_3 surface, with a binding energy of -0.69 eV. For this configuration, Fig. 4a shows the changes in the charge-density profile across the ferrocene-perovskite interface, suggesting that both the Fe metal centre and the Cp rings engage in significant electronic interactions with undercoordinated Pb. Second, adsorption of the ferrocene molecule results in the reduction of the work function by 1.01 eV (SI, Fig. S26 and Table S2), suggesting band bending at the perovskite surface, which agrees well with our previous experimental findings using Kelvin probe force microscopy.^{23,29} This is also in accord with the TAS results (Fig. 3f), which reveal longer hole polaron lifetimes in spiro-OMeTAD doped with strongly oxidising ferroceniums (Fig. S27 and Supplementary Note S1, SI).

Third, the simulated electronic density of states (DOS) (Fig. 4b) indicates that the neutral ferrocene modifies the electronic structure of the surface by introducing additional energy states within the band gap, which do not appear in the bulk DOS (Fig. S28). These results suggest that ferrocene forms hybridized states with undercoordinated surface Pb^{2+} , consistent with studies pertaining to interaction of neutral Fc with perovskite surfaces.^{23,29} Also, a small blue shift (0.03 eV) of the surface band gap was found, which indicates possible passivation of the perovskite surface, mitigating non-radiative

recombination centres. Finally, the ferrocene-surface hybridized states elevate the highest occupied energy level above the valence band maximum (VBM), which helps to account for the work function shift at the surface. As a result, these hybridized states serve as intermediate channels between the HOMO level of the Fc-doped spiro-OMeTAD layer and the VBM level of the perovskite, which would facilitate efficient hole extraction (illustrated schematically in Fig. 4c).

In summary, we have shown that the chemical structure of the metallocenium cation can be easily modified to tune its oxidation potential and strength through (i) substitution of the metal or (ii) fine-tuning of the Cp ring functionality. Our *ab initio* simulations suggest that the neutral ferrocene by-products and their influence on the perovskite (e.g. band bending, surface hybridized states, and passivation) collectively contribute to the enhanced hole extraction at the interface between the perovskite and the HTL layer as observed from the TAS experiments.

Application of ferrocenium dopants in n-i-p PSCs

To this point, we have demonstrated the flexibility afforded by ferrocenium dopants using spiro-OMeTAD as a technologically relevant molecular OSC. We next investigate the ferrocenium salt doping on PTAA and P3HT, archetypal examples of poly(triarylamine) and poly(thiophene) classes of OSCs, respectively (Fig. 5a). It has been reported that both PTAA and P3HT have similar values of $E_{\text{ox}}(\text{OSC})$ to spiro-OMeTAD, allowing both OSCs to be doped upon addition of $[\text{Fc}][\text{TFSI}]$, leading to a change in colour shown in Fig. 5b (inset) and the absorption profile (SI, Fig. S29).^{11,54,55} Confirmation of doping for both OSCs using $[\text{Fc}][\text{TFSI}]$ was made using EPR spectroscopy, presented in Fig. 5b and distinct changes in the ^1H NMR spectra arising from the presence of paramagnetic effects (SI, Fig. S30).



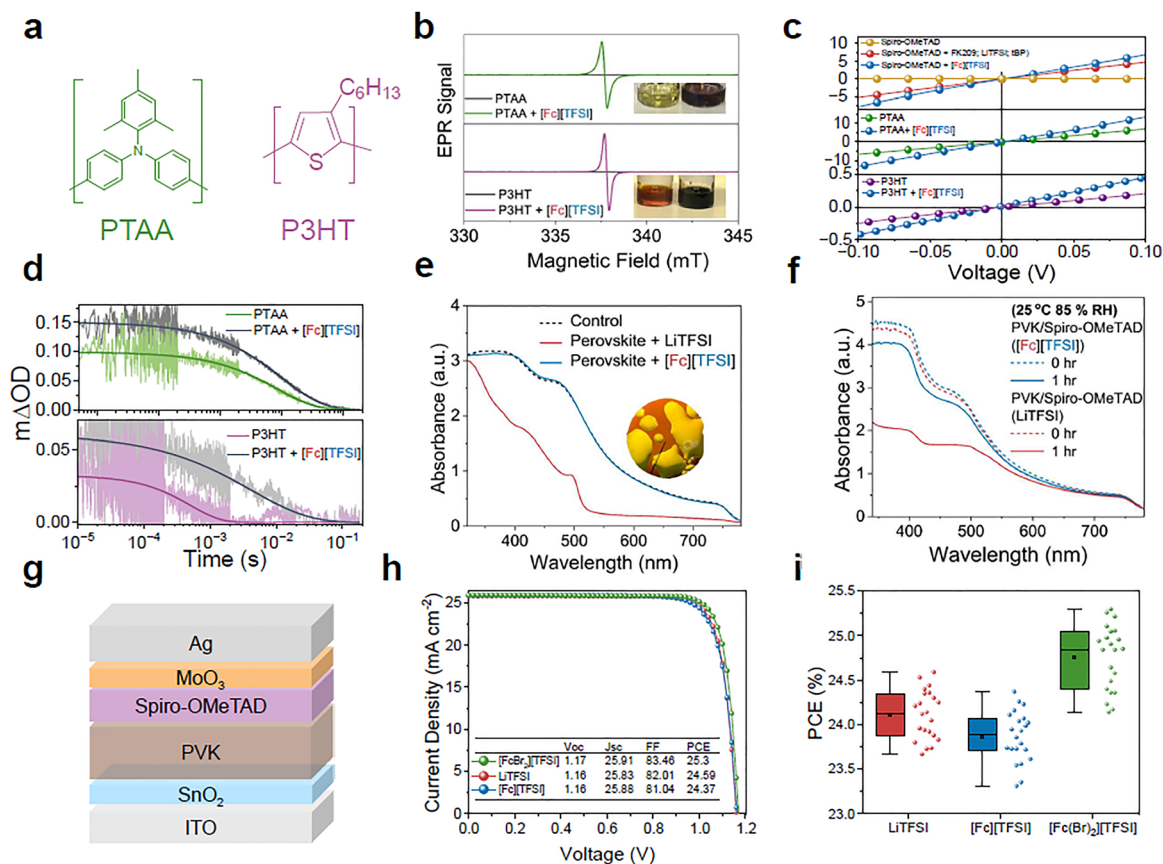


Fig. 5 Applicability of ferrocenium dopants in alternative OSCs and PSCs. (a) Chemical structures of poly(triarylamine) (PTAA) and poly(3-hexylthiophene) (P3HT). (b) EPR spectra of PTAA (above) and P3HT (below) with and without [Fc][TFSI] doping. (Inset) Photographs showing the colour change of PTAA and P3HT pre-doping (left) and post-doping (right). (c) $J-V$ characteristics of the ohmic region of spiro-OMeTAD (top), PTAA (centre), and P3HT (bottom) using an ITO/PEDOT:PSS/OSC/Au architecture with and without [Fc][TFSI] doping. Conductivity σ calculated using $I = \sigma AVd^{-1}$.⁵⁶ (d) μ s-TAS decays of the perovskite/HTL interface prepared with and without [Fc][TFSI] in PTAA (green) and P3HT (purple). (e) Absorbance spectra of perovskite substrates after interfacial contact with LiTFSI or [Fc][TFSI] for a period of 2 minutes. (Inset) Microscope photograph of LiTFSI-induced cation washout in the perovskite, forming yellow PbI_2 regions. (f) Absorbance spectra of perovskite substrates prepared with spiro-OMeTAD doped using LiTFSI + FK209 or [Fc][TFSI] under high humidity conditions (85% RH, 25 °C). (g) Device architecture schematic of n-i-p PSCs used to demonstrate ferrocenium doping of spiro-OMeTAD as an HTL. (h) Champion $J-V$ curves and (i) PCE statistical distribution of PSCs prepared using LiTFSI, [Fc][TFSI] or [Fc(Br)₂][TFSI].

¹⁹F NMR spectroscopy further confirmed the formation of both PTAA and P3HT TFSI salts, demonstrating that eqn (1) holds for different OSCs, provided E_{ox} of the ferrocenium centre is larger than the ionisation potential of the OSC (SI, Fig. S31). In all three OSCs tested, we observe improvements to the electrical conductivity (σ) upon doping with [Fc][TFSI], increasing from 1.6×10^{-10} to 2.3×10^{-5} S cm⁻¹, 3.7×10^{-4} to 7.2×10^{-4} S cm⁻¹ and 2.4×10^{-5} to 4.8×10^{-5} S cm⁻¹ for spiro-OMeTAD, PTAA and P3HT, respectively (Fig. 5c).⁵⁶ Similarly, TAS and time-resolved photoluminescence (TRPL) measurements on perovskite heterojunctions prepared with PTAA or P3HT HTLs show improved yields of hole injection post-doping, indicating enhanced OSC performance of the HTL (Fig. 5d and SI, Fig. S32).

To evaluate the stability of ferrocenium-based dopants against conventional LiTFSI, solid forms of both dopants were deposited on exposed perovskite substrates and the change in absorbance was measured (Fig. 5e). The hygroscopic LiTFSI samples quickly condensed water in as little as 120 seconds,

forming visible water droplets on the perovskite and producing yellow regions in the film (SI, Fig. S33). In these regions, the perovskite cation is removed, leaving behind PbI_2 as confirmed by absorbance spectroscopy.⁵⁷ In contrast, negligible changes occur to the perovskite upon contact with [Fc][TFSI], owing to the excellent air-stability of the ferrocenium salts when in the solid-state and the Cp rings increasing the hydrophobicity at the interface. We next consider the stability of MAPbI₃/doped spiro-OMeTAD photoactive layers following ageing under ISOS-D3 (RH = 85%) damp storage conditions. In these experiments, we observed a significant loss in the perovskite absorbance in the LiTFSI-doped films following 1 hour of ageing. In contrast, we observed only a minor change in the UV-vis spectra of [Fc][TFSI] doped samples under the same ageing conditions (Fig. 5f).⁵⁸ TAS experiments were further used to probe the yield of hole transfer in perovskite/doped spiro-OMeTAD films during storage under ISOS-D3 conditions. Comparing the evolution of ΔOD_{max} , we report a retention of 56% of the initial hole extraction yield after 96 hours in the [Fc][TFSI] doped films.



maximum yield of hole transfer (ΔOD_{\max}) (corresponding to the largest deviation in absorbance) was collected at $t = 1 \mu\text{s}$.

Mass spectrometry (MS). MS was conducted following recrystallisation and purification of the metallocenium salts. Direct analysis was performed using a Waters LCT Premier TOF mass spectrometer. The mass spectrometer operated in positive electrospray ionisation (ESI) mode with full MS scan. The mass range was from m/z 100 to 2000 with the following parameters: the source capillary was 2500 V, sample cone 35 V, desolvation temperature 350 °C and source temperature 120 °C. The TOF was calibrated with sulfadimethoxine $[\text{M} + \text{H}]^+$ with an m/z value of 311.0814 and leucine enkephalin $[\text{M} + \text{H}]^+$ with an m/z value of 556.2771.

Matrix-assisted laser desorption/ionisation. Mass spectrometry data were acquired in the chemistry mass spectrometry facility using a Shimadzu MALDI TOF. The instrument operated in positive linear mode in the mass range of 100–2000 m/z with 5 accumulated shots of 200 Hz laser repetition rate. The sample was prepared using a 2,5- α -cyano-4-hydroxycinnamic acid (CHCA) matrix. The laser wavelength was 355 nm and the power between 40 and 50 a.u.

Cyclic voltammetry (CV). Cyclic voltammetry was performed using a Gamry 1010E potentiostat using a 50 mL glass/PTFE chamber with a Luggin Capillary (Osilla). A three-electrode configuration of platinum ($\Phi = 2 \text{ mm}$) (work), platinum wire (counter) and silver/silver nitrate (0.1 M in ACN) was used. 2 mM of the sample was dissolved in 50 mL of acetonitrile electrolyte (0.1 M $[\text{NBu}_4\text{PF}_6]$) and degassed under N_2 for 5 minutes. Samples were swept in cycles at a scan rate of 100 mV s^{-1} unless specified. The potential was converted to a vacuum potential using the ionisation potential of Fc as 5.10 eV, as per the previous literature.

X-ray diffraction (XRD). Powder X-ray diffraction was measured as follows: diffraction patterns for metallocene powders were obtained using a PANalytical X'Pert Pro MRD diffractometer, where incident X-rays originated from a Cu $\text{K}\alpha$ X-ray source ($\lambda = 1.54 \text{ \AA}$) at 40 kV and 40 mA. The diffraction patterns were obtained over the 2θ range 10° – 50° in steps of 0.02° . Single crystal X-ray diffraction (SCXRD) data was obtained using an Agilent Xcalibur 3E diffractometer, and further experimental details of the SCXRD experiments are provided in the SI.

Density functional theory (DFT). All geometries were optimised using density functional theory with a CAM-B3LYP functional with Grimme's empirical dispersion correction (GD3).^{61,62} A 6-31G(d,p) basis set was used for all atoms in all calculations. Gibbs free energy of reaction (1) was calculated using:



$$\Delta G_{\text{r}}(\text{eqn (1)}) = [\Delta G(\text{spiro-OMeTAD}^+\text{Y}^-) + \Delta G(\text{Fc})] - [\Delta G(\text{spiro-OMeTAD}) + \Delta G(\text{Fc}^+\text{Y}^-)]$$

To calculate the ionic binding energy between the spiro-OMeTAD⁺ the following method was used:

$$\Delta G_{\text{r}}(\text{spiro-OMeTAD}^+\text{Y}^-) = [\Delta G(\text{spiro-OMeTAD}^+\text{Y}^-)] - [\Delta G(\text{spiro-OMeTAD}^+) + \Delta G(\text{Y}^-)]$$

For the bulk MAPbI_3 structure, *ab initio* calculations were performed using a plane-wave/pseudopotential DFT approach as implemented in the Vienna *Ab initio* Simulation Package (VASP), with valence electron configurations explicitly defined as: $1s^1$ (H), $2s^2 2p^2$ (C), $2s^2 2p^3$ (N), $2s^2 2p^4$ (O), $3s^2 3p^6 3d^7 4s^1$ (Fe), $5s^2 5p^5$ (I), and $5d^{10} 6s^2 6p^2$ (Pb). The generalized gradient approximation (GGA) exchange–correlation functionals of Perdew–Burke–Ernzerhof (PBE) was used. The Grimme's DFT-D3 dispersion correction term was added to all of our total energy calculations (apart from the validation simulations using $r^2\text{SCAN}$ and spin–orbital coupling). A kinetic energy cut-off of 520 eV and a Gaussian smearing of 0.01 were implemented for the self-consistent field (SCF) method calculations, with a convergence criterion of 1×10^{-6} eV. Spin-polarization was considered due to the presence of the iron atom. For geometry optimizations, a k -point grid of $4 \times 4 \times 4$ was used for the bulk system ($1 \times 1 \times 1$ for surface slabs). For electronic structure calculations, a finer $6 \times 6 \times 6$ k -point grid was used for the bulk system ($2 \times 2 \times 1$ for surface slabs). To obtain an accurate bulk tetragonal-phase MAPbI_3 structure, a $2 \times 2 \times 2$ supercell of the MAPbI_3 structure with random orientations of MA cations was generated using *ab initio* molecular dynamics (AIMD) with an on-the-fly machine-learning interatomic potential under NVT ensemble conditions at 300 K in VASP. The final configuration was fully relaxed from the dynamic structure and selected based on agreement with experimentally reported values for lattice constants ($a = b = 8.76 \text{ \AA}$, $c = 12.71 \text{ \AA}$), mean Pb–I bond length (3.19 \AA), and band gap energy (1.57 eV). The structural relaxation was terminated when all forces relaxed smaller than 1×10^{-2} . Such methods have been used successfully in recent related studies of perovskite halides.^{63–65}

Our PbI_2 -terminated (001) surface slab was constructed from the fully optimized $2 \times 2 \times 2$ tetragonal- MAPbI_3 supercell. A $2 \times 2 \times 3$ slab structure was constructed with a vacuum region of 20 \AA on top to avoid any spurious interactions between the periodic images. Starting from the DFT-optimized molecule-surface structure, AIMD simulations were carried out at 300 K for at least 10 ps under the NVT ensemble. To accurately describe the C–H and N–H vibrations, a time step of 0.5 fs was employed. To reduce the computational cost at each step, a reduced SCF convergence criterion of 1×10^{-4} eV and a Gaussian smearing width of 0.05 were used in the electronic calculations. Dipole moment correction was applied on both energies and forces for all surface simulations, with the dipole centre set at the midpoint of the slab. The binding energies were calculated as: $E_{\text{Binding}} = E_{\text{Tot}}^{\text{S+M}} - E_{\text{Tot}}^{\text{S}} - E_{\text{Tot}}^{\text{M}}$, where $E_{\text{Tot}}^{\text{S+M}}$, $E_{\text{Tot}}^{\text{S}}$, and $E_{\text{Tot}}^{\text{M}}$ are the total energies of surface-molecule, surface-only, and molecule-only in the same simulation box respectively. The ferrocene-surface hybridized states also appeared using the meta-GGA level functional $r^2\text{SCAN}$ and spin–orbital coupling, suggesting that the hybridized states were not artefacts from the GGA-level functional.



Conflicts of interest

The authors declare no other competing interests.

Data availability

Datasets are available from the corresponding author upon reasonable request.

The data supporting this article have been included as part of the supplementary information (SI). Supplementary information is available. see DOI: <https://doi.org/10.1039/d5ee05482f>.

CCDC 2479149 contains the supplementary crystallographic data for this paper.⁶⁶

Acknowledgements

S. A. H. and M. S. I. gratefully acknowledge funding from the Engineering and Physical Sciences Research Council (EPSRC, EP/X012344/1 and EP/X012484/1). T. W. thanks the Engineering and Physical Sciences Research Council (EPSRC, DTP EP/T51780X/1) for funding. Z. L. gratefully acknowledges funding from the Research Grants Council of Hong Kong, Innovation and Technology Fund (ITS/147/22FP, MHP/079/23), N. J. L. acknowledges funding from the Imperial College Sir Edward Frankland BP Endowment, the Imperial College Deep Tech Funding Scheme and the UKRI IAA project on “Organometallic-enhanced perovskite solar cells”.

References

- J. Blochwitz, M. Pfeiffer, T. Fritz and K. Leo, Low voltage organic light emitting diodes featuring doped phthalocyanine as hole transport material, *Appl. Phys. Lett.*, 1998, **73**, 729–731.
- J. J. Andre, *et al.*, Molecular semiconductors and junction formation: Phthalocyanine derivatives, *Synth. Met.*, 1987, **18**, 683–688.
- B. Maennig, *et al.*, Controlled p-type doping of polycrystalline and amorphous organic layers: Self-consistent description of conductivity and field-effect mobility by a microscopic percolation model, *Phys. Rev. B: Condens. Matter Mater. Phys.*, 2001, **64**, 195208.
- M. Pfeiffer, *et al.*, Doped organic semiconductors: Physics and application in light emitting diodes, *Org. Electron.*, 2003, **4**, 89–103.
- M. Ahles, R. Schmechel and H. von Seggern, n-type organic field-effect transistor based on interface-doped pentacene, *Appl. Phys. Lett.*, 2004, **85**, 4499–4501.
- Y. Hu, *et al.*, Doping Polymer Semiconductors by Organic Salts: Toward High-Performance Solution-Processed Organic Field-Effect Transistors, *ACS Nano*, 2018, **12**, 3938–3946.
- G.-H. Kim, L. Shao, K. Zhang and K. P. Pipe, Engineered doping of organic semiconductors for enhanced thermoelectric efficiency, *Nat. Mater.*, 2013, **12**, 719–723.
- W. Zhao, J. Ding, Y. Zou, C. Di and D. Zhu, Chemical doping of organic semiconductors for thermoelectric applications, *Chem. Soc. Rev.*, 2020, **49**, 7210–7228.
- Y. Xiong, *et al.*, Revealing the Impact of F4-TCNQ as Additive on Morphology and Performance of High-Efficiency Non-fullerene Organic Solar Cells, *Adv. Funct. Mater.*, 2019, **29**, 1806262.
- Y. Dong, *et al.*, Dopant-induced interactions in spiro-OMeTAD: Advancing hole transport for perovskite solar cells, *Mater. Sci. Eng., R*, 2025, **162**, 100875.
- F. M. Rombach, S. A. Haque and T. J. Macdonald, Lessons learned from spiro-OMeTAD and PTAA in perovskite solar cells, *Energy Environ. Sci.*, 2021, **14**, 5161–5190.
- M. Jha, *et al.*, Stability Study of Molecularly Doped Semiconducting Polymers, *J. Phys. Chem. C*, 2024, **128**, 1258–1266.
- Y. Yamashita, *et al.*, Efficient molecular doping of polymeric semiconductors driven by anion exchange, *Nature*, 2019, **572**, 634–638.
- J. Pan, *et al.*, Efficient molecular doping of polymeric semiconductors improved by coupled reaction, *Nat. Commun.*, 2024, **15**, 5854.
- M. Schwarze, *et al.*, Molecular parameters responsible for thermally activated transport in doped organic semiconductors, *Nat. Mater.*, 2019, **18**, 242–248.
- J. Meng, I. E. Castelli and Z. Lan, Heavy Doping-Induced Phase Segregation and Heterojunction Formation, *ACS Mater. Lett.*, 2025, **7**, 891–897.
- F. Deschler, *et al.*, Imaging of morphological changes and phase segregation in doped polymeric semiconductors, *Synth. Met.*, 2015, **199**, 381–387.
- I. Salzmann, G. Heimel, M. Oehzelt, S. Winkler and N. Koch, Molecular Electrical Doping of Organic Semiconductors: Fundamental Mechanisms and Emerging Dopant Design Rules, *Acc. Chem. Res.*, 2016, **49**, 370–378.
- G. Zhu, *et al.*, Unveiling the Critical Role of Oxidants and Additives in Doped Spiro-OMeTAD toward Stable and Efficient Perovskite Solar Cells, *ACS Appl. Energy Mater.*, 2022, **5**, 3595–3604.
- J. E. Rainbolt, *et al.*, Synthesis and characterization of p-type conductivity dopant 2-(3-(adamantan-1-yl)propyl)-3,5,6-trifluoro-7,7,8,8-tetracyanoquinodimethane, *J. Mater. Chem. C*, 2013, **1**, 1876–1884.
- P. K. Koech, *et al.*, Synthesis and Application of 1,3,4,5,7,8-Hexafluorotetracyanonaphthoquinodimethane (F6-TNAP): A Conductivity Dopant for Organic Light-Emitting Devices, *Chem. Mater.*, 2010, **22**, 3926–3932.
- Y. Karpov, *et al.*, Hexacyano-[3]-radialene anion-radical salts: a promising family of highly soluble p-dopants, *Chem. Commun.*, 2018, **54**, 307–310.
- F. Vanin, *et al.*, Modulating Perovskite Surface Energetics Through Tuneable Ferrocene Interlayers for High-Performance Perovskite Solar Cells, *Angew. Chem., Int. Ed.*, 2025, **64**, e202424041.
- Best Research-Cell Efficiency Chart | Photovoltaic Research | NREL. <https://www.nrel.gov/pv/cell-efficiency>.



